Dalton Transactions

PAPER

View Article Online
View Journal

Cite this: DOI: 10.1039/c5dt02171e

A combined experimental and computational study of novel nanocage-based metal–organic frameworks for drug delivery†

Jian-Qiang Liu,*[a] Xue-Feng Li,[b] Chu-Ying Gu,[a] Júlio C. S. da Silva,[c] Amanda L. Barros,[c] Severino Alves-Jr,[c] Bao-Hong Li,[a] Fei Ren,*[d] Stuart R. Batten[e] and Thereza A. Soares*[c]

Received 8th June 2015,
Accepted 7th October 2015

DOI: 10.1039/c5dt02171e

www.rsc.org/dalton

Three new metal organic frameworks (MOFs) with chemical formulae $[(CH_3)_2NH_2][Sm_3(L1)_2(HCOO)_2(DMF)_2(H_2O)]\cdot 2DMF\cdot 18H_2O$ (**1**), $[Cu_2(L2)(H_2O)_2]\cdot 2.22DMA$ (**2**) and $[Zn_2(L1)(DMA)]\cdot 1.75DMA$ were synthesized and structurally characterized. **1** and **2** show a classical **NbO**-like topology and have two types of interconnected cages. **3** exhibits an uncommon **zzz** topology and has two types of interconnected cages. These MOFs can adsorb large amounts of the drug 5-fluorouracil (5-FU) and release it in a progressive way. 5-FU was incorporated into desolvated **1**, **2** and **3** with loadings of 0.40, 0.42, and 0.45 g g^{-1}, respectively. The drug release rates were 72%, 96% and 79% of the drug after 96 hours in **1**, 120 hours in **2** and 96 hours in **3**, respectively. Grand Canonical Monte Carlo (GCMC) simulations were performed to investigate the molecular interactions during 5-FU adsorption to the three novel materials. The GCMC simulations reproduced the experimental trend with respect to the drug loading capacity of each material. They also provided a structural description of drug packing within the frameworks, helping to explain the load capacity and controlled release characteristics of the materials. 5-FU binding preferences to **1**, **2** and **3** reflect the diversity in pore types, chemistry and sizes. The calculated drug load is more related to the molecular properties of accessible volume V_{acc} than to the pore size.

Introduction

Metal–organic frameworks (MOFs) have drawn considerable attention in recent years due to promising applications in gas technology, catalysis, sensors, and electronic devices.[1–8] MOFs have also been applied to biomedical storage and release of drugs in biological environments.[2,9,10] These porous materials are promising candidates as drug delivery platforms due to features such as large surface area, tunable pore size and shape, adjustable composition and functionalization of pore surface, and intrinsic biodegradability.[2,10] In this scenario, Férey and co-workers have pioneered the use of MOFs for drug adsorption and release.[11] This concept has been expanded by the work of several other groups motivated by the development of new procedures of synthesis for obtaining new nanostructured porous materials with high potential for drug adsorption and controlled release, and low toxicity.[2,12–14] Rosi and co-workers have proposed the design of the denominated biomolecule-based metal–organic frameworks (bio-MOFs), where deoxyribonucleotides and amino acids are used as organic linkers and the inorganic part is composed of biocompatible metal ions.[15,16] This class of material exhibits good performance for the encapsulation of anionic drugs. MOFs containing amino-functionalized linkers have also been synthesized for application in the transport of pro-drugs based on metallodrugs.[17,18] Recently, it has been shown that MOFs can be produced for the incorporation and release of two different types of drugs.[19] This study has shown that a Ni-based MOF (CPO-27-Ni) can concomitantly incorporate nitric oxide and RAPTA-C drugs due to the different interaction sites between the MOF and the two adsorbates. This approach has great potential for application in drug delivery for combined thera-

[a]School of Pharmacy, Guangdong Medical University, Dongguan, 523808, P. R. China. E-mail: jianqiangliu8@gdmc.edu.cn
[b]School of Basic Medicine, Guangdong Medical University, Dongguan, 523808, P. R. China
[c]Department of Fundamental Chemistry, Federal University of Pernambuco, Cidade Universitária 50740-560 Recife, PE, Brazil. E-mail: thereza.soares@ufpe.br
[d]Department of Pharmacy, Nanfang Hospital, Southern Medical University, Guangzhou 510515, China. E-mail: paper_mail@126.com
[e]School of Chemistry, Monash University Victoria 3800, Australia and Department of Chemistry, Faculty of Science, King Abdulaziz University, Jeddah, Saudi Arabia

†Electronic supplementary information (ESI) available: Atomic parameters and topologies for GCMC simulations, TGA curves, X-ray powder diffraction data, IR spectra and 3D representations of the unit cell. CCDC 1060133, 1060134 and 1061360. For ESI and crystallographic data in CIF or other electronic format see DOI: 10.1039/c5dt02171e

pies. Despite progress in the synthesis, functionalization and application of biocompatible MOFs for drug delivery, there is only a limited understanding of drug adsorption and release processes at the molecular level. Such understanding requires the characterization of the three-dimensional structure and the chemical interactions for MOF drug complexes which have been constrained by experimental challenges such as the difficulties associated with the growing of mono-crystals, the possibility of adsorption on multiple sites, the presence of disordered solvent molecules and so on.[20–23]

Computational simulations can offer a unique insight into the nature of host–guest interactions at the atomic level. In the context of porous materials, the method of choice is the Grand Canonical Monte Carlo (GCMC) which has been extensively applied to simulate gas adsorption processes.[24–28] In the grand canonical ensemble, the number of particles in the system can vary whereas the chemical potential, volume and temperature are kept constant.[29,30] GCMC simulations generate configurational ensembles for which adsorption isotherms and isosteric heat of adsorption can be calculated and directly compared to measurements from adsorption experiments.[24,27–29] However, the use of GCMC simulations to investigate the adsorption of large molecules to porous materials remains challenging due to the requirement of the conformational sampling and fitting of fairly large and/or flexible molecules inside tight pores. Reported modeling studies on drug–MOFs remain rather scarce. For example, Bernini *et al.* combined computational simulations with available experimental data to describe the adsorption and release of ibuprofen in a series of MIL-based MOFs, providing thermodynamic and structural details of the process.[31] Horcajada *et al.* used periodic Density Functional Theory (DFT) calculations to investigate the most favorable conformation and adsorption sites of ibuprofen and busulfan on MIL-53(Fe). Vasconcelos *et al.* have performed molecular docking calculations to show that doxorubicin cannot fit within the ZIF-8 cage, and favors adsorption on the material surface.[32] Cunha *et al.* performed DFT calculations in combination with GCMC simulations to evaluate the uptake process of caffeine into MIL-53, MIL-100 and MIL-127 MOFs.[13]

We report here the synthesis and structural characterization of three novel MOFs with chemical formulae $[(CH_3)_2NH_2][Sm_3(L1)_2(HCOO)_2(DMF)_2(H_2O)]\cdot 2DMF\cdot 18H_2O$ (**1**), $[Cu_2(L2)(H_2O)_2]\cdot 2.22DMA$ (**2**) and $[Zn_2(L1)(DMA)]\cdot 1.75DMA$ (**3**) (H_4L1 = 2,6-di(3′,5′-dicarboxylphenyl)pyridine, H_4L2 = 2,5-di(3′,5′-dicarboxylphenyl)pyridine). The presence of large nanocage-based pores makes these frameworks promising candidates as drug delivery platforms. Therefore, GCMC simulations were performed for the adsorption of 5-fluorouracil (5-FU). This drug was chosen as a model due to its small size and clinical relevance for the treatment of several cancer types. The GCMC simulations show that the three frameworks can adsorb large amounts of 5-FU, which have been confirmed by experimental measurements of drug release. These experiments have also shown that 5-FU is released from the three frameworks in a progressive way.

Materials and methods

All reagents were purchased from commercial sources and used as received. IR spectra were recorded with a Perkin–Elmer Spectrum One spectrometer in the region 4000–400 cm^{-1} using KBr pellets. TGA was carried out with a Mettler–Toledo TA 50 under dry dinitrogen flux (60 mL min^{-1}) at a heating rate of 5 °C min^{-1}. X-ray powder diffraction (XRPD) data were collected on a Rigaku RU200 diffractometer at 60 kV, 300 mA for Cu K_α radiation (λ = 1.5406 Å), with a scan speed of 2 °C min^{-1} and a step size of 0.02° in 2θ.

X-ray crystallography

Room-temperature X-ray diffraction measurements were carried out on a Bruker SMART APEX diffractometer equipped with a graphite monochromated MoKα radiation (λ = 0.71073 Å) by using an ω-scan technique. The intensities were corrected for absorption effects by using SADABS.[34] The structures were solved by using SHELXL2014.[33] Absorption corrections were applied by using multi-non-hydrogen atoms, which were refined anisotropically. For **1** and **2**, the unit cell exhibited large regions occupied by solvent molecules. The solvent molecules could not be modeled. The SQUEEZE option in PLATON[35] was used to produce a set of solvent-free diffraction intensities. The nature and number of solvent molecules were established from CH&N elemental and thermogravimetric analyses. Crystallographic details and selected bond dimensions for **1–3** are listed in Tables 1 and 2. CCDC numbers: 1060133 and 1060134 for **1** and **2**, and 1061360 for **3**.

Synthesis

$[(CH_3)_2NH_2]$ $[Sm_3(L1)_2(HCOO)_2(DMF)_2(H_2O)]\cdot 2DMF\cdot 18H_2O$ (1). A mixture of $Sm(NO_3)_2\cdot 6H_2O$ (0.450 g, 0.1 mmol) and H_4L (0.015 g, 0.04 mmol) was dissolved in DMF (4 mL) in a screw-capped vial. Then, five drops of HNO_3 (65%, aq) were added into the mixture. The vial was capped and placed in an oven at 110 °C for 3 days. The resulting pale yellow single crystals were washed with absolute CH_3CH_2OH three times to give **1**. $C_{58}H_{94}N_7O_{43}Sm_3$ (2028.45). Calcd: C, 34.34; H, 4.67; N, 4.83. Found C, 34.25.; H, 4.55; N, 4.64. IR (KBr, cm^{-1}): 3458(vs); 2026(m); 1628(m); 1435(v); 1390(v); 1269(vs); 1183(m); 1107 (m); 1021(m); 917(vs); 778(vs); 715(vs); 657(vs); 454(m).

$[Cu_2(L2)(H_2O)_2]\cdot 2.22DMA$ (2). A mixture of $Cu(NO_3)_2\cdot 3H_2O$ (0.055 g, 0.2 mmol) and H_4L (0.021 g, 0.05 mmol) was dissolved in DMA (4 mL) in a screw-capped vial. Then, ten drops of HNO_3 were added into the mixture. The vial was capped and placed in an oven at 110 °C for 3 days. The resulting blue single crystals were washed with absolute CH_3CH_2OH three times to give **2**. $C_{29.89}H_{41}Cu_2N_{3.22}O_{12.22}$ (768.07). Calcd: C, 46.74; H, 5.38; N, 5.87. Found C, 46.35; H, 5.27; N, 5.78. IR (KBr, cm^{-1}): 3471(vs); 2368(m); 1623(vs); 1390(vs); 1051(vs); 998(m); 770(m); 572(m).

$[Zn_2(L1)(DMA)]\cdot 1.75DMA$ (3). The synthesis procedure was similar to that of **1** except that $Sm(NO_3)_2\cdot 6H_2O$ and DMF were replaced by $Zn(NO_3)_2\cdot 6H_2O$ (0.1 mmol) and DMA(4 mL). Anal. Calcd for $C_{32}H_{33.75}N_{3.75}O_{10.75}Zn_2$ (773.62), C, 49.68; H, 4.40;

Table 1 Crystal data and structure refinement information for novel framework structures

Complex	1	2	3
Empirical formula	$C_{58}H_{94}N_7O_{43}Sm_3$	$C_{29.89}H_{41}Cu_2N_{3.22}O_{12.22}$	$C_{32}H_{33.75}N_{3.75}O_{10.75}Zn_2$
Formula mass	2028.45	768.07	773.62
Crystal system	Cubic	Trigonal	Tetragonal
Space group	$Im\bar{3}$	$R\bar{3}m$	$P4/n$
a [Å]	38.3513(17)	18.6342(14)	27.4541(15)
b [Å]	38.3513(17)	18.6342(14)	27.4541(15)
c [Å]	38.3513(17)	37.709(3)	9.7375(5)
α [°]	90	90	90
β [°]	90	90	90
γ [°]	90	120	90
V [Å^3]	56 408(8)	11 339.7(19)	7339.4(6)
Z	24	9	8
d_{calcd} [g cm^{-3}]	1.433	1.012	1.400
$F(000)$	24 504	3588	3184
Reflections collected	175 427	23 422	69 414
$R_{(int)}$	0.0297	0.0529	0.0394
R_1, wR_2 [$I > 2\sigma(I)$]	0.0577, 0.1479	0.0359, 0.0950	0.0608, 0.1437
R_1, wR_2 (all data)	0.0756, 0.1699	0.0523, 0.1022	0.0818, 0.1552
GOF on F^2	1.079	0.955	1.093

Table 2 Selected bond distances (Å) and angles (°) of structures 1–3

Structure 1			
Sm1–O1	2.330 (8)	Sm1–O8	2.331 (8)
Sm1–O1w	2.520 (18)	Sm1–O10	2.579 (6)
Sm1–O12	2.590 (2)	Sm1–O11	2.61 (2)
Sm2–O7	2.351 (7)	Sm2–O2	2.371 (7)
Sm2–O10	2.413 (4)	Sm2–O6	2.423 (7)
Sm2–O9	2.433 (6)	Sm2–O5	2.433 (7)
Sm2–O3	2.444 (7)	Sm2–O4	2.459 (8)
O1–Sm1–O1	78.5 (4)	O1–Sm1–O8	77.7 (4)
O8–Sm1–O8	124.2 (6)	O1–Sm1–O1w	136.1 (3)
O10–Sm1–O12	149.6 (3)	O7–Sm2–O2	86.4 (2)
O2–Sm1–O6	154.8 (2)	O7–Sm2–O3	154.7 (2)
Structure 2			
Cu1–O1	1.9448(14)	Cu1–O2	1.9437(14)
Cu1–O1w	2.121(2)	Cu1–Cu1	2.6283(6)
O1–Cu1–O1	88.67(10)	O1–Cu1–O2	167.90(6)
O2–Cu1–O2	88.58(10)	O1–Cu1–O1w	94.51(8)
O2–Cu1–O1w	97.60(8)		
Structure 3			
Zn1–O7	1.953(2)	Zn1–O5	1.999(3)
Zn1–O1	2.006(3)	Zn1–O8	2.112(3)
Zn1–O4	2.127(3)	Zn2–O6	1.911(3)
Zn2–O3	1.917(3)	Zn2–O2	1.935(3)
Zn2–O9	1.964(6)		
O7–Zn1–O5	121.35(12)	O7–Zn1–O1	105.96(12)
O5–Zn1–O1	132.54(12)	O8–Zn1–O4	170.73(11)
O3–Zn2–O2	114.21(14)	O2–Zn2–O9	110.8(4)

N, 6.79. Found C, 49.01; H, 4.29; N, 6.55. IR (KBr, cm^{-1}): 3072(vs); 2832(m); 1644(v); 1574(vs); 1411(v); 1349(vs); 1248(vs); 783(vs); 721(vs); 636(m).

Drug loading and release

To load 5-fluorouracil (5-FU) into the pores of desolvated **1–3**, the dehydrated frameworks were dispersed in a 5-FU containing methanol solution (25 mL) and stirred for up to 3 days when the maximum drug load was attained. These steps were followed by extensive centrifugation and sample washing with chloroform to obtain the drug-loaded frameworks. The amount of 5-FU adsorbed into the porous solids was estimated by Fourier-Transform Infrared (FTIR) and UV-Vis absorption spectroscopy at 265 nm and. Experiments were performed in quadruplicate and drug payloads 5-FU was calculated according to the equation:

$$\text{5-FU (wt\%)} = \text{5-FU (mg)/hydrated materials (mg)\%}$$

Samples of the respective frameworks after the incorporation of 5-FU were loaded into a dialysis bag (MWCO = 1000), which were dialyzed against 500 mL of PBS buffer solution (pH 7.4) at room temperature. During each time interval, 1 mL of solution was taken out, and 1 mL of fresh PBS buffer was added. The amount of 5-FU released from the solids was determined by UV-Vis adsorption spectroscopy at an excitation wavelength of 265 nm.

Computational details

The adsorption process of the 5-Fluorouracil (5-FU) molecule to **1**, **2** and **3** was investigated using Grand Canonical Monte Carlo simulations (GCMC) at 300 K. Interactions of 5-FU with the frameworks were described by a potential composed of van der Waals and Coulomb components. van der Waals interactions were treated using the Lennard–Jones (LJ) potential and atomic parameters taken from the UFF force field[36] (details in the ESI†). The mixed LJ parameters for 5-FU/MOF and 5-FU/5FU interactions were calculated using the Lorentz–Berthelot mixing rules, and LJ interactions beyond 12 Å were neglected. Coulomb interactions were calculated using atomic partial charges obtained *via* the charge equilibration (EQeq) method proposed by Snurr and co-workers.[37] Partial charges for 5-FU molecules were calculated at the B3LYP/6-311**G level of theory (see the ESI†) *via* the ChelpG[38] method as

implemented in Gaussian 09 program.[39] From these atomic charges, the electrostatic interactions were computed using the Ewald sum method.[40,41] GCMC simulations were carried out with 1×10^7 equilibration steps and 2×10^7 production steps. The configuration-bias Monte Carlo method[42,43] was used for trial MC moves involving insertion and deletion of 5-FU molecules. Trial moves related to the rotation and translation of 5-FU molecules were performed randomly. Potential maps used in configuration-biased GCMC simulations were calculated using a grid spacing of 0.1 Å and a cut off of 160 kJ mol^{-1} for interaction energy. All MC moves included in this study were treated with equal probability. The framework was treated as rigid and vibrational and angular deformations of 5-FU molecules were neglected. All GCMC simulations were performed using the Multipurpose Simulation Code.[44] Pore size distributions (PSD), pore volume, accessible surface area and crystal density were calculated using the MC algorithm implemented in the Zeo++ program.[45,46] Structural properties were calculated using a charge probe of 1.2 Å of radius. Drug loading was calculated from the excess number of drug molecules. The excess number of molecules was calculated according to the equation:

$$n = n^{\mathrm{abs}} - V^{g}\rho$$

where V^g is the pore volume of the adsorbent and ρ is the molar density of the bulk gas phase calculated by using the Peng–Robinson equation of state. n^{abs} is the absolute number of molecules obtained from the GCMC simulations performed at a pressure of 1 atm. Critical properties of 5-FU molecules required for the calculation of molar density of the bulk phase were taken from previously estimated values.[47] The values of the critical temperature, critical pressure and critical volume used in these calculations were 1056.17 K, 58.59 bar and 248.0 cm^3 mol^{-1}, respectively. The pore volume of frameworks investigated was computed using the Monte Carlo method as implemented in the Zeo++ code.[45,46]

Results and discussion

X-ray structure of compound 1

Although the topology of framework **1** is similar to previously reported compounds, we describe here the new structural features.[51] The structure of **1** contains Sm_3 clusters in which the metal atoms are connected by carboxylate groups from L ligands and a μ_4 formate anion (Fig. 1). The L ligands in turn coordinate to three Sm_3 clusters, two *via* a single carboxylate group each, and one through two carboxylate groups (see Fig. S1† for geometries around Sm centers). Hence, the ligands act as 3-connecting nodes, while the Sm_3 cluster is coordinated by eight carboxylates from six L ligands. This generates a 3D network (Fig. S2†) with two different 3-connecting ligand nodes (there are two crystallographically different L ligands which, in the underlying network, are also topologically different) and 6-connecting Sm_3 nodes. It has a $(4{\cdot}6^2)$-$(4{\cdot}6^2)(4^2{\cdot}6^7{\cdot}8^6)$ topology.

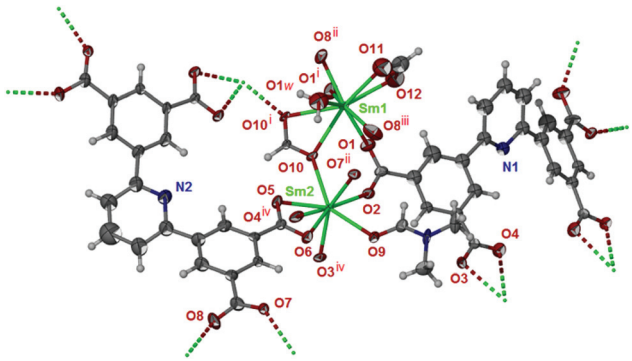

Fig. 1 ORTEP plot of the coordination environment of Sm(III) ions and its connectivity L1 ligands in **1**, C grey, O red, N blue, Sm green. The uncoordinated water and DMF molecules are not shown (symmetric codes: (i) *x*, −*y*, *z*; (ii) *y*, *z*, *x* (iii) *x*, −*y*, −*z*; (iv) *x*, *y*, −*z*).

The topology can be best thought of as interconnected cages of two types, one smaller and one larger. The smaller cage contains twelve 6-connecting nodes bridged by twelve 3-connecting nodes (one such cage is highlighted by pink bonds in Fig. 2(a)). Notably, the cage contains a "belt" of four 4-membered rings around the middle. These 4-membered rings are defined by two 3-connected and two 6-connected nodes, which are connected to each other by sharing their 6-membered nodes. Two of the 4-membered rings contain one type of 3-connecting node (light green in Fig. 2(a)), while the other contains the other type of 3-connecting node (dark green in Fig. 2(a)). This belt is then capped by two more 4-membered rings (containing the light green 3-connecting nodes) which are held in place by connections between their 6-connecting nodes and the light green nodes of the belt, and by bonds from both the dark green nodes of the belt and the light green nodes of the capping rings to additional 6-connecting nodes.

Therefore, each one of the small cages contains six 4-membered rings, four in a central belt and two capping above and below this belt, in a distorted octahedral arrangement. These cages are connected to each other *via* the sharing of the four rings with the light green nodes between adjacent cages, meaning that each cage is connected to four neighbors. As adjacent cages are orientated approximately perpendicular to each other (Fig. 2(a)), the cages connect together in a **NbO**-type fashion (Fig. 2(b)). This generates a larger cavity (blue sphere in Fig. 2(b)), which corresponds to the larger cage of the underlying 3,3,6-connected net mentioned earlier. The larger cage, highlighted by the blue bonds in Fig. 2(a), contains six 4-membered rings joined together by connections between 3-connecting nodes of one ring to 6-connecting nodes of adjacent rings, and has the same topology as the sodalite cage. Notably, the 3-connecting nodes in this larger cage are all exclusively of the dark green variety.

X-ray structure of compound 2

The structure of **2** is similar to that of the compound $\{[Cu_2(L2)(H_2O)_2]{\cdot}x\mathrm{solvent}\}_n$ that has been reported by Champness

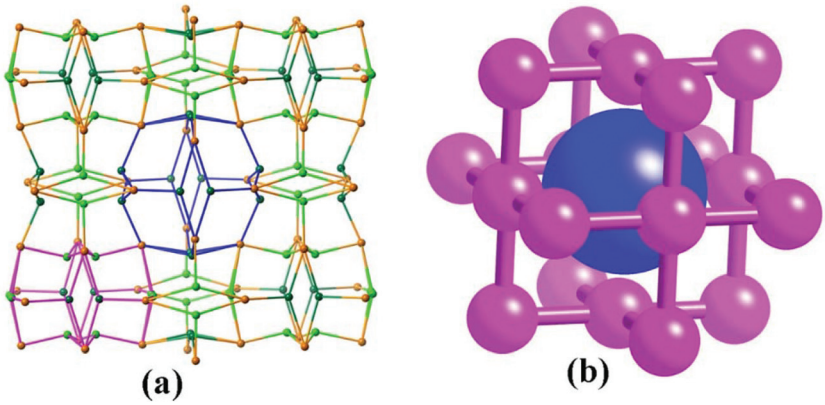

Fig. 2 (a) Schematic representation of the 3D network formed in the structure of **1**. Light green and dark green nodes represent the two topologically different 3-connecting ligand nodes, while the orange nodes represent the 6-connecting Sm_3 clusters. A small cage is highlighted at the bottom right by the pink bonds; a large cage is highlighted in the centre by the blue bonds. (b) Schematic representation of the way the **NbO**-like arrangement of the smaller cages (blue sphere) generates the larger cages (pink sphere).

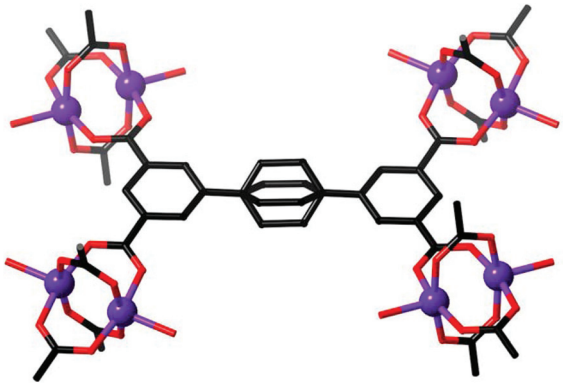

Fig. 3 Local geometry of ligand and metal coordination environments in structure **2**, C black, O red, Cu pink. The central ring of the L2 ligand is disordered over two positions.

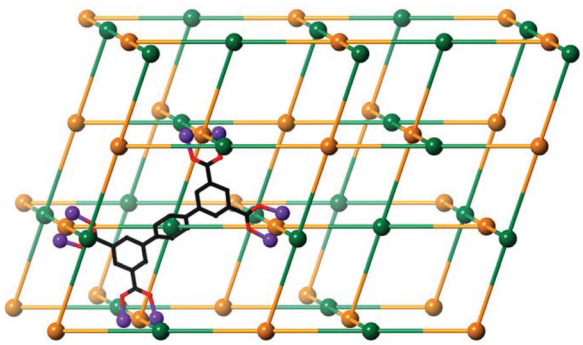

Fig. 4 Schematic representation of the 3D **NbO**-like network in structure **2**. Green nodes represent the ligands, while the orange nodes represent the Cu_2 binuclear clusters. A single ligand of the chemical structure with coordinated Cu atoms is shown in the bottom left corner. For clarity, only one position of the disordered central ring is shown.

et al.[48] The structure of **2** contains dinuclear Cu_2 clusters displaying the classic copper acetate motif, in which pairs of Cu metals are bridged by carboxylate groups from four separate ligands (Fig. 3). The five-coordinate geometries of the metals are completed by coordinated water ligands. The L ligands in turn coordinate to four separate Cu_2 dimers. The 3D network can be simplified by treating both the Cu_2 dimers and L2 ligands as 4-connecting nodes. This reduces the structure to a network with an **NbO**-like topology (Fig. 4); both the Cu_2 dimers and L ligands act as the square planar nodes (all four carboxylate groups of the ligand are close to coplanar).

X-ray structure of compound 3

The structure of **3** contains linear Zn_4 clusters bridged by L1 ligands; all clusters and all L1 are equivalent. The Zn_4 cluster contains two different Zn atoms (Fig. 5(a)). The central Zn atoms are 5-coordinate and bridged to each other by two L carboxylate groups. The two outer Zn atoms are then each connected to a central Zn *via* three bridging L1 carboxylate groups. The coordination spheres of the tetrahedral outer Zn atoms are then completed by a disordered DMA ligand. Each Zn_4 cluster is thus coordinated by eight carboxylate groups from six L1 ligands. Each L1 is, in turn, coordinated to three Zn_4 clusters, once each to two and twice to the third (Fig. 5(b)). Based on this connection, an open framework with 3D infinite intersected channels was formed (Fig. 5(c)). The dimensions of the largest channels are approximately 5.1 × 5.6 Å along the *c* axis. This generates a 3,6-connected net with a **zzz**-like topology (Fig. 6). The net is closely related to the common rutile net (**rtl**), which has the same Schläfli symbol $((4{\cdot}6^2)_2(4^2{\cdot}6^{10}{\cdot}8^3))$, however it contains two different types of channels. One is topologically the same as those in the rutile net (highlighted in pink in Fig. 6), where opposing 6-mem-

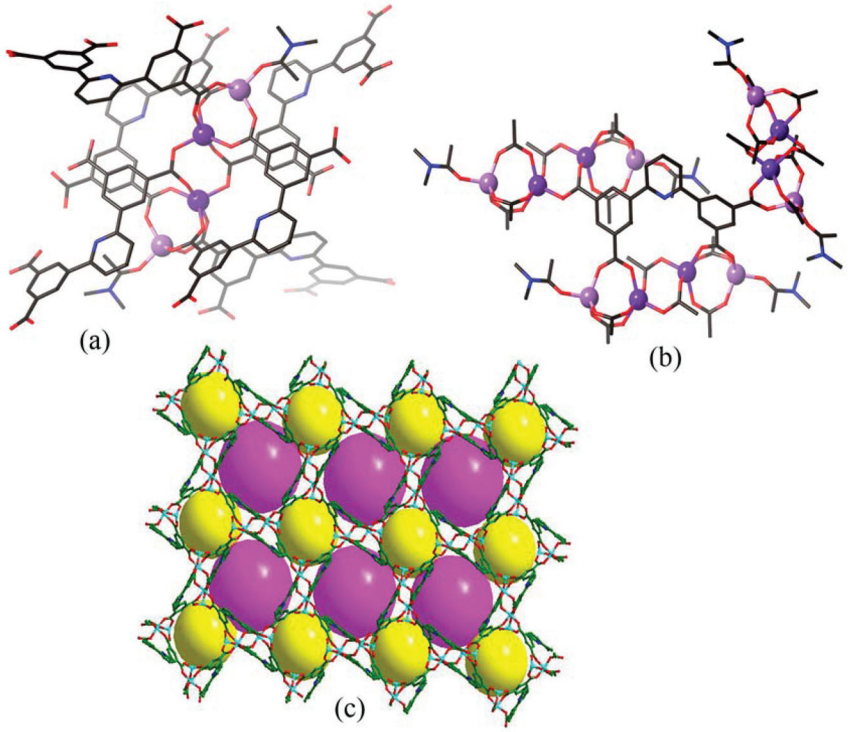

Fig. 5 Local coordination geometries of (a) the Zn_4 cluster, and (b) the L ligand in the structure of **3**. C black, N blue, O red, Cu pink. For clarity, only one position of the disordered DMA ligand is shown, and (c) two kinds of nanoscale cages in 3, the pink spheres represent the void space inside the large cages and the yellow spheres represent the small void space inside the small cages.

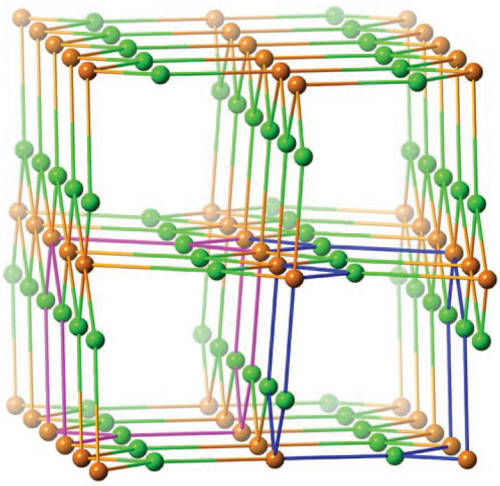

Fig. 6 The underlying **zzz** net in the structure of **3**. Green nodes represent the 3-connecting ligands, while orange nodes represent the 6-connected Zn_4 clusters. Opposing 6-membered rings in a rutile-like channel are highlighted in pink; spiralling 6-membered rings in a helical channel are highlighted in blue.

bered rings are connected directly to each other, while in the other (highlighted in blue) the 6-membered rings spiral along the channel (there are equal numbers of helical channels of opposite handedness).

Drug adsorption measurements

The framework structure of **1** is anionic with H_2O and the $(CH_3)_2NH_2^+$ cation (the product of DMF decomposition) as well as DMF residing in the channels as shown by elemental analysis, thermogravimetric analysis and the consideration of charge balance. The TGA data (Fig. S3†) for **1** reveal a weight loss of 20.3% from room temperature to 240 °C, corresponding to the loss of the free DMF and water molecules (*ca.* 21.3%). The as-synthesized blue-green crystalline samples of **2** lose solvent rapidly over 25–110 °C, resulting in a deep purple-blue crystalline material. Desolvated **2** can be stabilized until 115 °C. The total observed weight loss based on the removal of DMA molecules in the first step was around 16.6% (cal. 17.1%) from 30 to 115 °C. For **3**, in the first step from 31.5 to 190 °C, the observed weight loss is 26.5%, which corresponds to the release of DMA molecules (cal. 28.9%).

The unusually large cages of the three porous structures led us to examine its drug release capability. 5-FU was selected because of its size, which was small enough to be incorporated into the cavity of **1–3**. Before its use as a drug delivery carrier, Samples **1–3** were activated (see Fig. S4†). Then, adsorption of anti-cancer 5-FU was carried out by impregnating **1–3** under stirring in 5-FU containing ethanol solutions. As evidenced by PXRD, 5-FU containing sample maintains its crystallinity (Fig. S4†), thus, the drug encapsulation did not alter the structure of these materials. It suggests that a slight shrinkage/swelling of the structures have taken place after the removal of

solvent molecules or encapsulation of drug molecules. The slight shrinkage of the structure may cause the disappearance of the strong diffraction peak at low angle reflections in **1** and **3**.[2b] This was confirmed by N_2 adsorption analyses showing that the BET surface area significantly decreases upon drug molecule loading (see the ESI Fig. S5†).[48,51] Incorporation of the drug molecule during the adsorption process has also been confirmed by Fourier transformed infrared spectroscopy (FTIR) (Fig. S6†). The characteristic peaks of –O–C–O– groups between 1660 and 1355 cm^{-1} are observed. The adsorption band at about 1240 cm^{-1} may be due to the fluorine atom on the ring. The absorption bands in the 820–550 cm^{-1} regions may be assigned to the C–F deformations.[49] Furthermore, the very strong and broad absorption band at *ca.* 3300–4000 cm^{-1} should be derived from OH stretching (maybe mixing with the N–H band) because of the existence of water molecules in the porous materials.

UV-vis absorption spectroscopy has been used to determine the effective storage capacity (see the ESI†). To reach a maximal drug loading, the 5-FU to porous solid relative ratio and contact time were tested. After the trivial tests, the best results were achieved when **1′–3′** were soaked for 3 days in a 20 mL ethanol solution with a 5-FU to **1′–3′** weight ratio of 1 : 3. 5-FU was incorporated into **1′–3′** with loadings of 0.40, 0.42, and 0.45 g g^{-1}, respectively. 5-FU loading into **1′** is a little lower than that of $\{NH_2(CH_3)_2[Zn(TATA)_{2/3}]\cdot 3DMF\cdot H_2O\}_n$ as reported by Sun and co-workers, but it is higher than that of Cu(pi)-PEG5k polymer.[49,50] However, 5-FU loading into **2** is higher that of the aforementioned two compounds.

Drug release experiments were performed by dialyzing the drug-loaded **1′–3′** in the PBS buffer solution (PBS = phosphate buffered saline pH 7.4) at 37 °C.[52] PXRD performed before and after 5-FU release shows that the crystal structure remains basically the same after the drug delivery (Fig. S4†). As shown in Fig. 7, the drug release rates were 72%, 96% and 79% of drug release after 96 hours in **1′**, 120 hours in **2′** and 96 hours in **3′**, respectively. In **1′**, three stages related to the drug release could be distinguished. Around 31% of the loaded drug was released during the initial burst release (24 hours). After that, there is a much flatter release curve up to 48 hours. However, for **2′**, around 45% of the loaded drug was released during the initial burst release (24 hours) and 51% was released in the latter two stages. As for **3**, it has the similar drug releasing behavior to **2**. Around 41% of the loaded drug was released

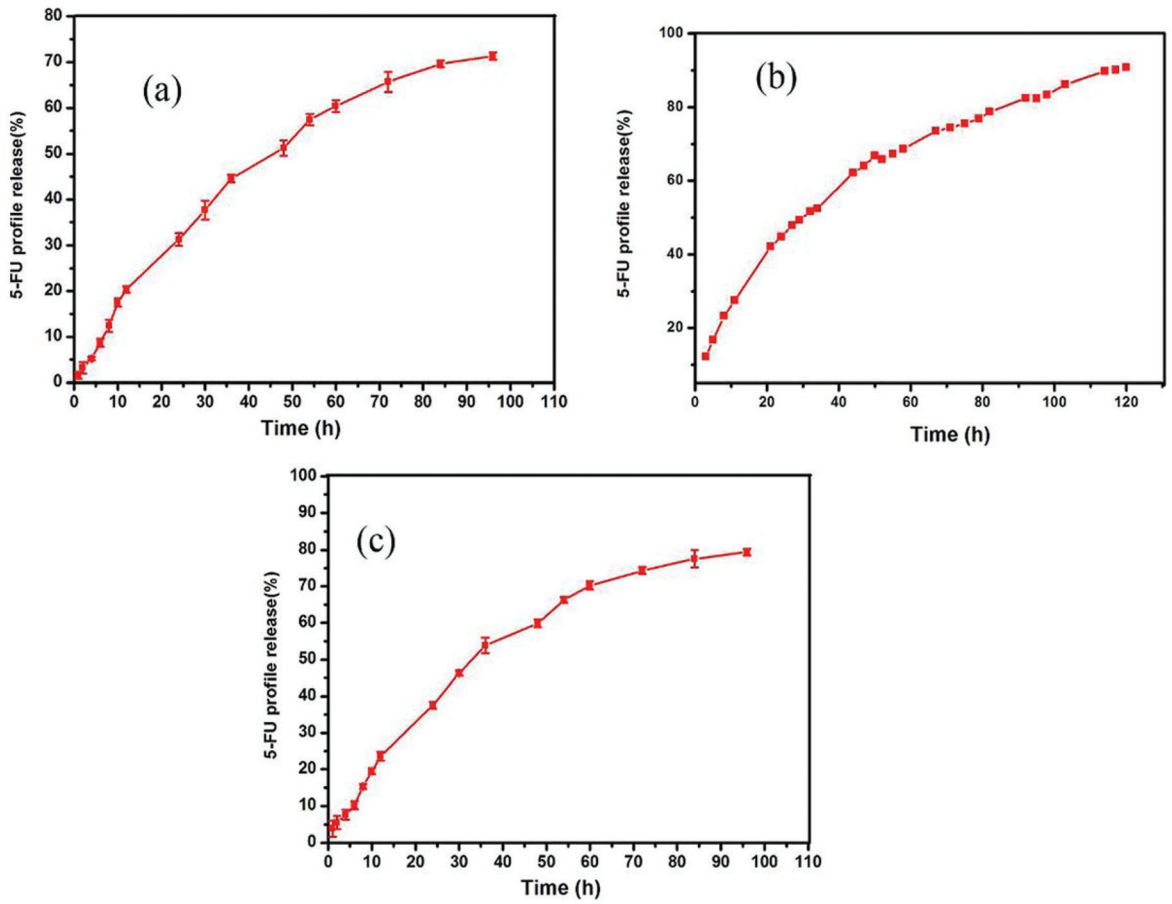

Fig. 7 Release profile of the 5-FU from the drug-loaded materials **1–3** in PBS buffer at 37 °C as determined by UV-vis absorption spectroscopy (% 5-FU *vs.* time).

Table 3 Structural properties of the Zn, Cu and Sm MOFs. Accessible surface area A_{asa}, pore volume V_p, accessible volume, maximum pore size D_{max}, crystal density ρ_{crys}, maximum calculated and measured drug loading and payloads (%wt)

System	A_{asa} ($m^2\ g^{-1}$)	V_p (A^3)	V_{acc} ($cm^3\ g^{-1}$)	D_{max} (Å)	ρ_{crys} ($g\ cm^{-3}$)	Calc. loading ($g\ g^{-1}$)	Exp. loading ($g\ g^{-1}$)	%wt calc.	%wt exp.
1 (SmMOF)	1815.3	16 471.4	0.272	16.14	1.07	0.27	0.40	27.0	40.0
2 (CuMOF)	2163.3	1794.4	0.096	6.40	1.19	0.25	0.42	25.0	42.0
3 (ZnMOF)	2136.1	2594.7	0.366	12.30	0.95	0.28	0.45	28.0	45.0

during the initial burst release (24 hours). As mentioned above, two different sizes of nanoscale cages exist in **1–3**. Their windows in **1** are 4.4 × 4.1 and 5.5 × 5.0 Å (see Fig. S2†), while their windows in **2** are 4.2 × 4.6 and 5.8 × 7.3 Å and in **3** are 4.3 × 4.5 and 6.4 × 7.8 Å (see Fig. S7†). Thus, only one window is larger than the size of the drug molecule (5.3 × 5.0 Å) in **1–3**. For each type cage from **1–3**, two circumstances may occur for the guest. For those drug molecules approaching the pores, the forces are dominated by the host–guest interactions from weak interactions (such as hydrogen bonds and packing interactions) between 5-FU and the skeleton of the organic ligand. Therefore, the strength of the force relies on the size of the cages and chemical feature of pores. For those drug molecules far away from the pores, the forces are mainly from intermolecular interactions between 5-FU molecules. Based on the above-mentioned structural distinctions, the windows of **2–3** are larger than that of compound **1**, which could be related to different loading contents. Furthermore, considering the difference in window size of the larger cages in **1** and **2**, 5-FU located in the pores of larger cages would be released preferentially with respect to those hosted into the smaller cages, which exhibit different release characteristics. As mentioned above, the 5-FU incorporated in the three frameworks is not fully released at once; the release of the residual ~10–20% took as long as 4 d. This can be attributed to host–guest interactions such as those between the amine group of 5-FU and the coordinative unsaturated metal center Sm/Cu/Zn in the frameworks, and π–π packing interactions between rings of 5-FU and the organic part of the frameworks).[2a] The host–guest interactions were further addressed *via* computational simulations of 5-FU adsorption to the frameworks as discussed in the following subsection.

Computational simulations of 5-FU adsorption

The amount of drug per porous material or drug loading is one of the main factors of interest in the use of MOFs for controlled drug release. We have used GCMC simulations to investigate the adsorption of 5-FU to **1**, **2** and **3** at the molecular level. These simulations were used to determine the preferential binding sites of the 5-FU in the porous materials, to estimate the maximum drug adsorption capacity of each material, and to propose a molecular mechanism for drug adsorption and release.

Selected structural parameters were calculated from the atomic coordinates of the three MOFs (Table 3). Structural features and the chemical nature of the pores are two important factors related to the capacity of a given material to adsorb molecules. Structural details about porous materials can be obtained from the analysis of the pore size distribution (PSD), which gives information about the amount of void space exists within a certain pore size or the porosity of a given material (Fig. 8). As can be observed, all three frameworks show distinct pore morphologies with varying pore distribution sizes (Fig. 8). **1** exhibits a bimodal distribution of pore sizes (Fig. 9) whereas **2** shows a pseudo-unimodal pattern (Fig. 10). **3** presents two well defined pores. The smaller pore has a cylindrical shape with a diameter of *ca.* 10.3 Å where the Zn^{2+} cations are easily accessible to interact with 5-FU. The larger pore has a square shape with a diameter of *ca.* 12.3 Å where the metallic ion is made less exposed by the presence of coordinating carboxylate groups from the organic linker (Fig. 11). The X-ray structure of **2** shows the presence of one microporous window between the main pores (Fig. 10). Only the main pore (~6.4 Å) is large enough to fit 5-FU (Fig. 8). **1** has also two pores with different dimensions (*ca*. 9.7 Å and 16.14 Å), but a similar chemical environment (Fig. 9). Pairs of organic linkers are positioned along the extension of both pore channels such as gates, which may hinder the entry/exit of 5-FU. The two pores differ in what concerns the horizontal (D_{max} 9.7 Å) or vertical (D_{max} 16.14 Å) placement of such gates (Fig. 8). Hence, the set of crystallographic and PSD data shows more intricate pore morphologies and volume voids for **1** and **2**.

GCMC simulations were performed to gain insight into the adsorption mechanism of 5-FU to **1**, **2**, and **3**. Among other information, the analysis of configurations generated from GCMC simulations can provide details about the binding site location of the drug molecules within the framework pores. Regarding the adsorption process of 5-FU to **3**, our results suggest that the binding of 5-FU to **3** should occur in two steps. Initially 5-FU molecules fill up the larger pore, forming well-structured aggregates (Fig. 11). Once the larger pores are occupied, 5-FU molecules bind to the smaller pore albeit in much smaller numbers (Fig. 11). The nature of the interactions between 5-FU and **3** governs such a binding pattern. In the larger pore, van der Waals interactions are the major forces driving 5-FU aggregation and its interaction with the aromatic rings in the organic linker. In contrast, electrostatic interactions between 5-FU molecules and Zn^{2+} cations are the major binding factors in the smaller pore. In the latter, 5-FU molecules do not form aggregates, and the pore volume is only partially filled with drug molecules (Fig. 11). 5-FU molecules adsorb unspecifically to mesopores in **1**, following a single

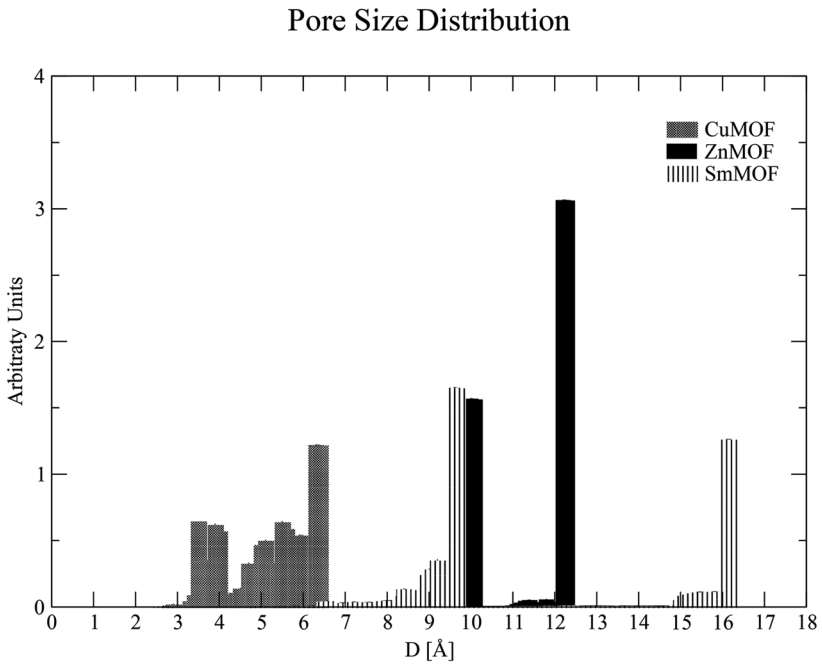

Fig. 8 Pore size distributions for structures **1** (SmMOF), **2** (CuMOF) and **3** (ZnMOF).

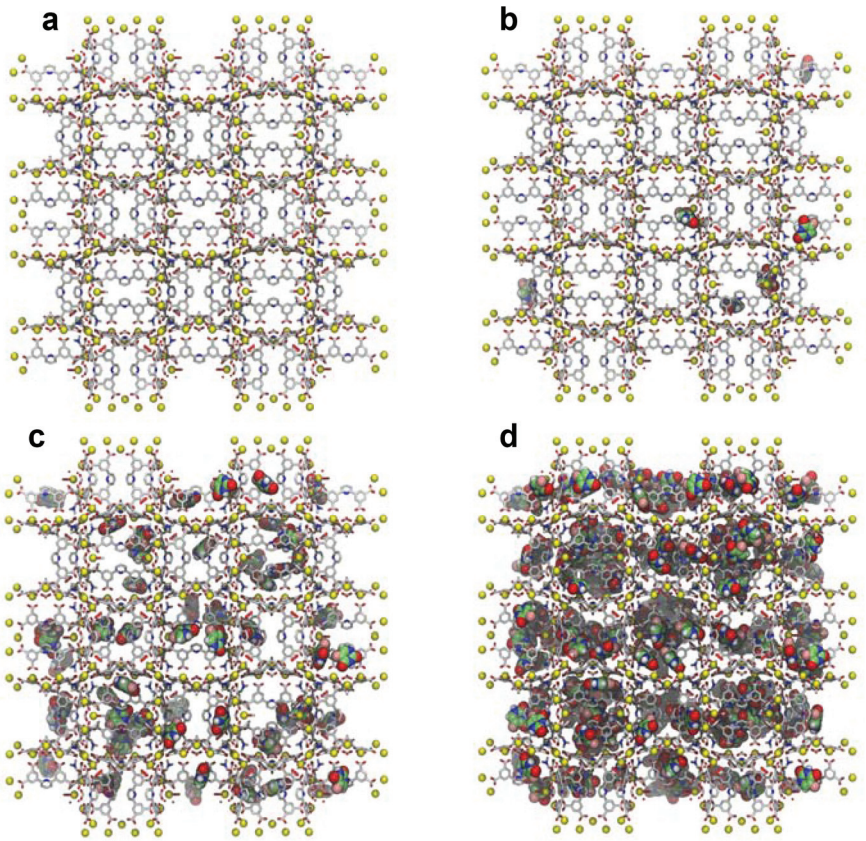

Fig. 9 Sequential snapshots taken from the GCMC simulation of the adsorption of 5-FU into **1**. 5-FU atoms are shown in van der Waals representation (C in green, F in pink, N in blue, O in red and H in white). Atoms of the organic linkers of compound **1** are shown in licorice representation (C in white, O in red and N in blue). Yellow spheres represent the Sm atoms.

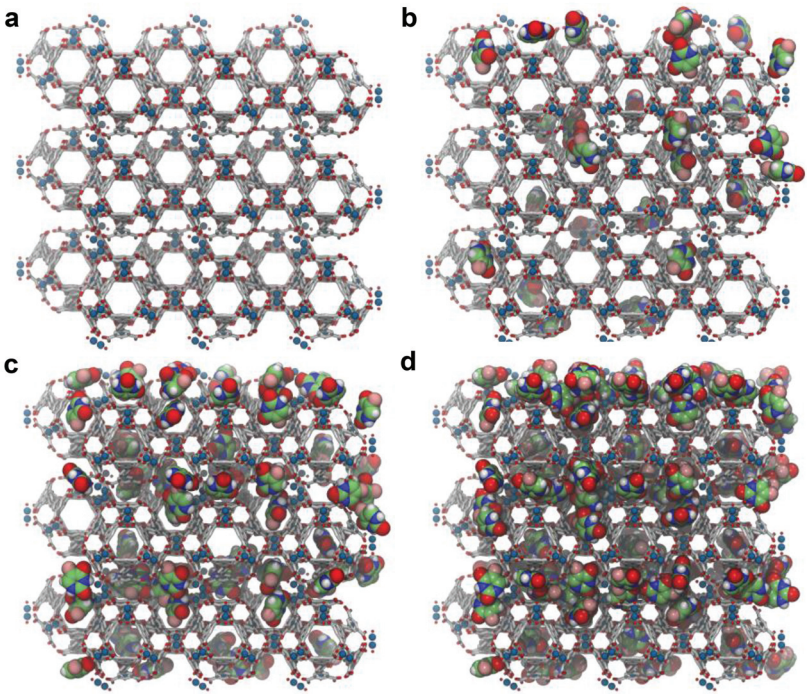

Fig. 10 Sequential snapshots taken from the GCMC simulation of the adsorption of 5-FU into **2**. 5-FU atoms are shown in van der Waals representation (C in green, F in pink, N in blue, O in red and H in white). Atoms of the organic linkers of compound **2** are shown in licorice representation (C in white and O in red). Light blue spheres represent the Cu atoms.

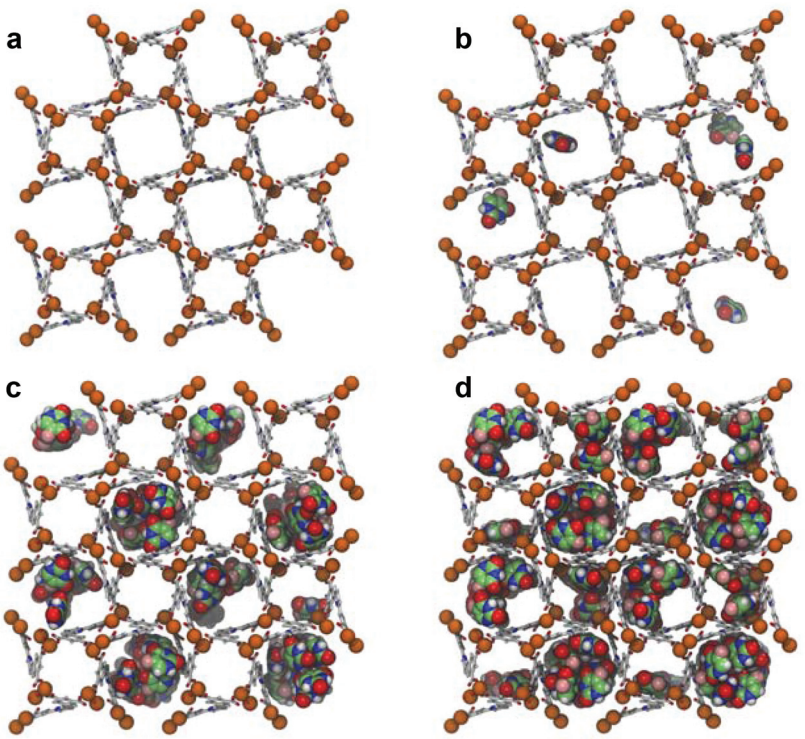

Fig. 11 Sequential snapshots taken from the GCMC simulation of the adsorption of 5-FU into **3**. 5-FU atoms are shown in van der Waals representation (C in green, F in pink, N in blue, O in red and H in white). Atoms of the organic linkers of compound **3** are shown in licorice representation (C in white, O in red and N in blue). Orange spheres represent the Zn atoms.

binding regime. Likewise for **2**, this has only one pore type large enough to incorporate 5-FU molecules. In both frameworks, 5-FU binds predominantly through electrostatic interactions with the metal ions and the carboxylate groups from the organic linkers (Fig. 9 and 10).

Two common features emerged from the GCMC simulations of 5-FU adsorption to **1**, **2**, and **3**. First, different 5-FU molecules make extensive intermolecular interactions upon confinement into the respective pores (Fig. 9–11). These interactions result from the presence of four hydrogen donor–acceptor sites in the pyrimidine group, which allows for a highly packed and structured arrangement of 5-FU molecules within pores. Second, the three frameworks exhibit an analogous adsorption capacity for 5-FU molecules despite their rather distinct structures and pore dimensions (Table 3). This is shown by computer simulations and experimental measurements (the deviation between experimental and theoretical loading values will be discussed afterwards). How structurally distinct frameworks exhibit nearly undistinguishable 5-FU load capacity?

An approach to understand the drug loading behavior of porous materials is to relate it to structural properties (*e.g.* surface area, density of material, pore size and available pore volume) (Table 3). **2** is the densest material (ρ_{crys} = 1.19 g cm^{-3}), has the smallest accessible volume per gram of material (V_{acc} = 0.096 cm^3 g^{-1}) and the smallest pore size structure (D_{max} = 6.40 Å) among the frameworks considered here. It has also the largest accessible surface area A_{asa}. Comparatively, **1** is less dense (ρ_{crys} = 1.07 g cm^{-3}), has the smallest accessible surface area (A_{asa} = 1815.3) of the three frameworks, a larger accessible volume per gram of material (V_{acc} = 0.272 cm^3 g^{-1}), and the largest pore dimension (D_{max} = 16.14 Å). **3** is the material with the lowest crystal density (ρ_{crys} = 0.95 g cm^{-3}), the highest accessible volume per gram (0.366 cm^3 g^{-1}), and the second larger accessible surface area (A_{asa} = 2136.1 m^2 g^{-1}). In the GCMC simulations of **2**, 5-FU binds inside the pore but also onto the framework surface (Fig. 10). In this material, the pore dimension restricts the number of drug molecules that can be accommodated across the pore diameter, and imposes a linear arrangement of these molecules along the pore channel. This is in contrast to simulations of **1** and **3**, which have lower density, smaller surface area and larger accessible volume compared to **2**. In these frameworks, 5-FU binds exclusively within the respective pores (Fig. 9 and 11).

A tentative molecular mechanism for the release of 5-FU from **1–3** is proposed based on the comparison between the GCMC simulations and the drug release profiles for these materials (Fig. 7). It should be mentioned that GCMC simulations do not offer direct information on time-dependent phenomena. Hence, the proposed molecular mechanism relies solely on the Boltzmann-averaged occupation rates of 5-FU with respect to different pores in the same framework. Three different stages are distinguished in the drug delivery profile for **1** and **3**. The first stage corresponds to the initial burst when there is a rapid release of the drug. At this stage, *ca.* 20% to 25% of 5-FU is released in 12 h from **3** and **1**, respectively (Fig. 7). In the remaining stages, 5-FU is progressively released as shown by the flattening of the profile curves. The drug release profiles of **1** and **3** are nearly undistinguishable during the first stage of the process (Fig. 7). Afterwards, 5-FU is released from **1** at slower rates compared to **3**. In **3**, 5-FU molecules in the form of aggregates interact with the large pore mainly *via* van der Waals interactions and with the small pore through electrostatic interactions with the metallic center (Fig. 11). The different nature of these interactions implies that 5-FU will be released first, and in sizeable amounts, from the large pore (*via* disruption of the short ranged van der Waals interactions) and then from the smaller pore at slower rates. In the case of **1**, 5-FU bound outside the pore gate can readily diffuse into the bulk solution as opposed to molecules inside the pore whose diffusion will be hindered or reduced by the gate (linkers) (Fig. 9). Compound **2** exhibits a rather distinct drug release profile from those measured for **1** and **3** (Fig. 7). In fact, its release curve shows two regimes: an initial burst in the first 12 h, followed by the uniform and steady release of 5-FU. Based on the GCMC simulations, the initial burst can be associated with the excess of 5-FU molecules adsorbed on the framework surface. The subsequent release stages can be connected to the slower diffusion of 5-FU molecules from **2** pores. Due to the small pore size of **2**, 5-FU molecules are arranged in a linear manner along the pore channel (Fig. 10). Such an arrangement can lead to the steady release of 5-FU observed in the drug release measurements (Fig. 7).

It should be mentioned that the calculated loading values are on average 40% lower than the experimentally measured ones (Table 3). Differences between experimental and calculated values within the same order of magnitude have been previously reported from adsorption studies involving different frameworks and drugs.[13,31] The discrepancy between calculated and experimental values can arise from diffusional issues during the pore filling process by drug molecules, which cannot be captured directly from GCMC simulations. It can also result from the inaccuracies in the experimental loading measurements. The experimental protocol relies on certain assumptions (*e.g.* drug solubility, porous material activation and solvent–drug competition for binding sites in the material) that are not easily ascertained. Further, experimental measurements are made indirectly from the excess of drug in solution, whereas the GCMC simulations quantify the number of drug molecules bound in pores of the material. Despite these limitations, our theoretical results indicate that the GCMC method reproduces drug loading values in MOFs within the same order of magnitude of experimental values while offering a microscopic, structure-based perspective of the adsorption process.

Conclusions

The present study reports on the experimental and computational characterization of three novel MOFs as drug delivery

platforms. The elucidation of the respective 3D structures revealed the presence of large nanocage-based pores. This structural feature was explored *via* GCMC simulations with the goal to identify a suitable drug for incorporation. GCMC simulations suggested that the anti-cancer drug 5-fluorouracil (5-FU) could adsorb to the three frameworks in high loads. The computational estimates were confirmed by drug adsorption experiments: 5-FU can be incorporated into desolvated **1**, **2** and **3** with loadings of 0.40, 0.42, and 0.45 g g^{-1}, respectively. Furthermore, 5-FU is released from these frameworks in a progressive manner with release rates of 72%, 96% and 79% after 96 hours in **1**, 120 hours in **2** and 96 hours in **3**, respectively. Our findings show that the combined experimental–computational approach is a powerful strategy for the efficient identification and incorporation of bioactive compounds in novel porous materials.

Acknowledgements

This work was partially supported by grants from the National Natural Science Foundation of China (Grant 21201044), the Chinese Training Plan of Guangdong Province Outstanding Young Professors in Higher Education Institutions (Grant YQ2013084), the Brazilian National Counsel of Technological and Scientific Development, CNPq (Grant PVE-400193/2013-2) and CAPES (Grant BioMol-230380046302014-35). JCSS acknowledges a post-doctoral fellowship from CNPq. TAS and SAJ are productivity fellows in research from CNPq. Prof. S. W. Ng is acknowledged for the refinement of structural data. The experimental measurements have been carried out by the Chinese team and the computational simulations by the Brazilian team. Science and Technology Planning Project of Guangdong Province (2014A010105026).

Notes and references

1 R. B. Getman, Y.-S. Bae, C. E. Wilmer and R. Q. Snurr, *Chem. Rev.*, 2012, **112**, 703–723.
2 (*a*) P. Horcajada, R. Gref, T. Baati, P. K. Allan, G. Maurin, P. Couvreur, G. Férey, R. E. Morris and C. Serre, *Chem. Rev.*, 2012, **112**, 1232–1268; (*b*) V. Agostoni, T. Chalati, P. Horcajada, H. Willaime, R. Anand, N. Semiramoth, T. Baati, S. Hall, G. Maurin, H. Chacun, K. Bouchemal, C. Martineau, F. Taulelle, P. Couvreur, C. Rogez-Kreuz, P. Clayette, S. Monti, C. Serre and R. Gref, *Adv. Healthcare Mater.*, 2013, **2**, 1630–1637.
3 (*a*) L. E. Kreno, K. Leong, O. K. Farha, M. Allendorf, R. P. Van Duyne and J. T. Hupp, *Chem. Rev.*, 2012, **112**, 1105–1125; (*b*) S. H. Li, M. L. Han, G. Z. Liu, L. F. Ma and L. Y. Wang, *RSC Adv.*, 2015, **5**, 17588–17591; (*c*) G. L. Li, G. Z. Liu, L. F. Ma, L. X. Xin, X. L. Li and L. Y. Wang, *Chem. Commun.*, 2014, **50**, 2615–2617.
4 J.-R. Li, J. Sculley and H.-C. Zhou, *Chem. Rev.*, 2012, **112**, 869–932.
5 M. P. Suh, H. J. Park, T. K. Prasad and D.-W. Lim, *Chem. Rev.*, 2012, **112**, 782–835.
6 M. Yoon, R. Srirambalaji and K. Kim, *Chem. Rev.*, 2012, **112**, 1196–1231.
7 K. Sumida, D. L. Rogow, J. A. Mason, T. M. McDonald, E. D. Bloch, Z. R. Herm, T.-H. Bae and J. R. Long, *Chem. Rev.*, 2012, **112**, 724–781.
8 C. Wang, T. Zhang and W. Lin, *Chem. Rev.*, 2012, **112**, 1084–1104.
9 P. Horcajada, T. Chalati, C. Serre, B. Gillet, C. Sebrie, T. Baati, J. F. Eubank, D. Heurtaux, P. Clayette, C. Kreuz, J.-S. Chang, Y. K. Hwang, V. Marsaud, P.-N. Bories, L. Cynober, S. Gil, G. Ferey, P. Couvreur and R. Gref, *Nat. Mater.*, 2010, **9**, 172–178.
10 S. Keskin and S. Kızılel, *Ind. Eng. Chem. Res.*, 2011, **50**, 1799–1812.
11 G. Férey, C. Mellot-Draznieks, C. Serre, F. Millange, J. Dutour, S. Surblé and I. Margiolaki, *Science*, 2005, **309**, 2040–2042.
12 R. C. Huxford, J. Della Rocca and W. Lin, *Curr. Opin. Chem. Biol.*, 2010, **14**, 262–268.
13 D. Cunha, M. Ben Yahia, S. Hall, S. R. Miller, H. Chevreau, E. Elkaïm, G. Maurin, P. Horcajada and C. Serre, *Chem. Mater.*, 2013, **25**, 2767–2776.
14 W. J. Rieter, K. M. Pott, K. M. L. Taylor and W. Lin, *J. Am. Chem. Soc.*, 2008, **130**, 11584–11585.
15 J. An, S. J. Geib and N. L. Rosi, *J. Am. Chem. Soc.*, 2009, **131**, 8376–8377.
16 C.-L. Chen and N. L. Rosi, *Angew. Chem., Int. Ed.*, 2010, **49**, 1924–1942.
17 K. M. L. Taylor-Pashow, J. Della Rocca, Z. Xie, S. Tran and W. Lin, *J. Am. Chem. Soc.*, 2009, **131**, 14261–14263.
18 J. Della Rocca, D. Liu and W. Lin, *Acc. Chem. Res.*, 2011, **44**, 957–968.
19 S. Rojas, P. S. Wheatley, E. Quartapelle-Procopio, B. Gil, B. Marszalek, R. E. Morris and E. Barea, *CrystEngComm*, 2013, **15**, 9364–9367.
20 F. Gandara and T. D. Bennett, *IUCrJ*, 2014, **1**, 563–570.
21 G.-L. Li, G.-Z. Liu, L.-F. Ma, L.-Y. Xin, X.-L. Li and L.-Y. Wang, *Chem. Commun.*, 2014, **50**, 2615–2617.
22 J. L. C. Rowsell, E. C. Spencer, J. Eckert, J. A. K. Howard and O. M. Yaghi, *Science*, 2005, **309**, 1350–1354.
23 Y. Kubota, M. Takata, R. Matsuda, R. Kitaura, S. Kitagawa, K. Kato, M. Sakata and T. C. Kobayashi, *Angew. Chem., Int. Ed.*, 2005, **44**, 920–923.
24 T. Düren, L. Sarkisov, O. M. Yaghi and R. Q. Snurr, *Langmuir*, 2004, **20**, 2683–2689.
25 K. S. Walton, A. R. Millward, D. Dubbeldam, H. Frost, J. J. Low, O. M. Yaghi and R. Q. Snurr, *J. Am. Chem. Soc.*, 2008, **130**, 406–407.
26 Z. Xiang, D. Cao, J. Lan, W. Wang and D. P. Broom, *Energy Environ. Sci.*, 2010, **3**, 1469–1487.
27 R. Babarao and J. Jiang, *Langmuir*, 2008, **24**, 6270–6278.
28 Q. Yang, C. Zhong and J.-F. Chen, *J. Phys. Chem. C*, 2008, **112**, 1562–1569.

29 T. Duren, Y.-S. Bae and R. Q. Snurr, *Chem. Soc. Rev.*, 2009, **38**, 1237–1247.
30 D. Dubbeldam, A. Torres-Knoop and K. S. Walton, *Mol. Simul.*, 2013, **39**, 1253–1292.
31 M. C. Bernini, D. Fairen-Jimenez, M. Pasinetti, A. J. Ramirez-Pastor and R. Q. Snurr, *J. Mater. Chem. B*, 2014, **2**, 766–774.
32 I. B. Vasconcelos, T. G. da Silva, G. C. G. Militao, T. A. Soares, N. M. Rodrigues, M. O. Rodrigues, N. B. da Costa, R. O. Freire and S. A. Junior, *RSC Adv.*, 2012, **2**, 9437–9442.
33 G. G. M. Sheldrick, *SHELXTL NT Version 5.1. Program for Solution and refinement of Crystal Structures*, University of Göttingen, 1997.
34 Bruker AXS, *SAINT Software reference Manual*, Madison, WI, 1998.
35 A. L. Spek, *J. Appl. Crystallogr.*, 2003, **36**, 7–13.
36 A. K. Rappe, C. J. Casewit, K. S. Colwell, W. A. Goddard and W. M. Skiff, *J. Am. Chem. Soc.*, 1992, **114**, 10024–10035.
37 C. E. Wilmer, K. C. Kim and R. Q. Snurr, *J. Phys. Chem. Lett.*, 2012, **3**, 2506–2511.
38 C. M. Breneman and K. B. Wiberg, *J. Comput. Chem.*, 1990, **11**, 361–373.
39 G. M. J. Frisch, W. Trucks, H. B. Schlegel, G. E. Scuseria, M. A. Robb, J. R. Cheeseman, G. Scalmani, V. Barone, B. Mennucci, G. A. Petersson, H. Nakatsuji, M. Caricato, X. Li, H. P. Hratchian, A. F. Izmaylov, J. Bloino, G. Zheng and D. J. F. Sonnenberg, J. L. M. Hada, M. Ehara, K. Toyota, R. Fukuda, J. Hasegawa, M. Ishida, T. Nakajima, Y. Honda, O. Kitao, H. Nakai, T. Vreven, J. A. Montgomery Jr., J. E. Peralta, F. Ogliaro, M. Bearpark, J. J. Heyd, E. Brothers, K. N. Kudin, V. N. Staroverov, R. Kobayashi, J. Normand, K. Raghavachari, A. Rendell, J. C. Burant, S. S. Iyengar, J. Tomasi, M. Cossi, N. Rega, J. M. Millam, M. Klene, J. E. Knox, J. B. Cross, V. Bakken, C. Adamo, J. Jaramillo, R. Gomperts, R. E. Stratmann, O. Yazyev, A. J. Austin, R. Cammi, C. Pomelli, J. W. Ochterski, R. L. Martin, K. Morokuma, V. G. Zakrzewski, G. A. Voth, P. Salvador, J. J. Dannenberg, S. Dapprich, A. D. Daniels, Ö. Farkas, J. B. Foresman, J. V. Ortiz, J. Cioslowski, and D. J. Fox, *W. C. Gaussian 09, Revision C.01*, 2009.
40 M. P. Allen and D. J. Tildesley, *Computer Simulation of Liquids (Oxford Science Publications) SE – Oxford science publications*, Oxford University Press, 1989.
41 H. Dufner, S. M. Kast, J. Brickmann and M. Schlenkrich, *J. Comput. Chem.*, 1997, **18**, 660–676.
42 M. N. Rosenbluth and A. W. Rosenbluth, *J. Chem. Phys.*, 1955, **23**, 356.
43 J. I. Siepmann and D. Frenkel, *Mol. Phys.*, 1992, **75**, 59–70.
44 A. Gupta, S. Chempath, M. J. Sanborn, L. A. Clark and R. Q. Snurr, *Mol. Simul.*, 2003, **29**, 29–46.
45 T. F. Willems, C. H. Rycroft, M. Kazi, J. C. Meza and M. Haranczyk, *Microporous Mesoporous Mater.*, 2012, **149**, 134–141.
46 R. L. Martin, B. Smit and M. Haranczyk, *J. Chem. Inf. Model.*, 2012, **52**, 308–318.
47 F. J. Ramos, R. Mazarro, A. de Lucas Martínez and J. F. Rodríguez, in Study of the phase equilibrium in binary systems anticancer drug-carbon dioxide, 10th International Symposium on Supercritical Fluids (ISSF), 2012.
48 X. Lin, J. Jia, X. Zhao, K. M. Thomas, A. J. Blake, G. S. Walker, N. R. Champness, P. Hubberstey and M. Schröder, *Angew. Chem., Int. Ed.*, 2006, **45**, 7358–7364.
49 C.-Y. Sun, C. Qin, C.-G. Wang, Z.-M. Su, S. Wang, X.-L. Wang, G.-S. Yang, K.-Z. Shao, Y.-Q. Lan and E.-B. Wang, *Adv. Mater.*, 2011, **23**, 5629–5632.
50 D. Zhao, S. Tan, D. Yuan, W. Lu, Y. H. Rezenom, H. Jiang, L.-Q. Wang and H.-C. Zhou, *Adv. Mater.*, 2011, **23**, 90–93.
51 B. Liu, W. P. Wu, L. Hou and Y. Y. Wang, *Chem. Commun.*, 2014, **50**, 8731–8734.
52 T. Wang, F. Chai, Q. Fu, L. Zhang, H. Liu, L. Li, Y. Liao, Z. Su, C. Wang, B. Duan and D. Ren, *J. Mater. Chem.*, 2011, **21**, 5299–5306.